AIAA JOURNAL
Vol. 45, No. 2, February 2007

Low-Frequency Acoustic Shielding by the Silent Aircraft Airframe

Anurag Agarwal* and Ann P. Dowling†
University of Cambridge, Cambridge, CB2 1PZ England, United Kingdom

DOI: 10.2514/1.19351

The Silent Aircraft airframe has a flying-wing design with a large wing planform and a propulsion system embedded in the rear of the airframe with intake on the upper surface of the wing. In the present paper, boundary-element calculations are presented to evaluate acoustic shielding at low frequencies. Besides the three-dimensional geometry of the Silent Aircraft airframe, a few two-dimensional problems are considered that provide some physical insight into the shielding calculations. Mean-flow refraction effects due to forward-flight motion are accounted for by a simple time transformation that decouples the mean-flow and acoustic-field calculations. It is shown that a significant amount of shielding can be obtained in the shadow region where there is no direct line of sight between the source and observer.

I. Introduction

THE "Silent Aircraft Initiative" is a project funded by the Cambridge-MIT Institute (CMI). Its aim is to discover ways of reducing aircraft noise to the point where it would be virtually imperceptible to people outside the airport perimeter in a typical urban environment. The present design of the Silent Aircraft is in the form of a flying wing with a large wing planform and a propulsion system that is embedded in the rear of the airframe with intake on the upper surface of the wing. Thus, a large part of the forward-propagating noise from the intake duct of the engines is shielded by the wing from observers on the ground.

Acoustic shielding estimates of noise from engines placed above a wing have been obtained by a few investigators in the past, experimentally and numerically, for both tube-and-wing and flying-wing aircraft configurations. For example, Jeffery and Holbeche [1] studied the acoustic shielding from a full-scale Hadley–Page 115 delta-winged aircraft in flight by centrally mounting a powerful acoustic whistle above the wing. They also performed experiments on a model scale aircraft mounted in a wind tunnel. They observed significant amount of shielding in the shadow region. They developed a simple model based on diffraction from a sharp-edged semi-infinite plate to predict the noise underneath the wing. Clark and Gerhold [2] experimentally investigated the noise shielding by a three-engine blended-wing-body (BWB) model. A high-frequency broadband point source was placed in the nacelles of the engines. They observed shielding in excess of 20 dB for the overall sound pressure level (OASPL) in the forward sector of the shadow region. The amount of shielding in the aft sector was relatively smaller, of the order of 10 dB. This is because both exhaust and inlet-radiated noise contributed to their result. Gerhold et al. [3] used a simple wedge-shaped wing with a triangular planform and a point source mounted in a nacelle above the wing to compare experimental results with a numerical model. They used a boundary integral method to perform low-frequency calculations and found good qualitative agreement with the experimental results. Ricouard et al. [4] studied the shielding of fan noise by the main wing of a scaled model tube-and-wing aircraft. In their experiments, the engine was mounted over the tail wing. In this situation shielding is effective only in certain directions underneath the wing, along which there is no direct line of sight between the engine-intake and observers on the ground. All these experimental investigations show a significant amount of shielding in the shadow zone underneath the aircraft. In the present authors' opinion, numerical solutions for realistic aircraft models so far have yielded only qualitative results and provide little physical insight into the acoustic shielding solutions. Most theoretical models developed so far use diffraction theories based on acoustic scattering from a semi-infinite plate, which have a limited range of validity. Also, most models and numerical simulations have ignored mean-flow refraction effects.

In the present paper, low-frequency acoustic shielding estimates are obtained from a point monopole source placed above simple two-dimensional geometries and a three-dimensional Silent Aircraft airframe. The analysis accounts for mean-flow refraction effects due to forward-flight motion and provides a framework for incorporating realistic acoustic sources. The two-dimensional models provide some physical insight into acoustic shielding calculations. For example, these models help explain the effect of various parameters such as wing thickness, edge curvatures, source frequency, etc., on the amount of acoustic shielding. These models also help in identifying the relevant length and frequency scales of the problem, which is useful in developing simple analytical models.

Acoustic shielding effects can be calculated by solving an external acoustic scattering problem. Acoustic waves generated by the engines are refracted by the mean flow past the moving aircraft. Considerable simplifications to this problem can be made for low-Mach number flows (where $|\boldsymbol{M}|^2$ is negligible in comparison with unity, $\boldsymbol{M}$ being the Mach number) that can be assumed to be homentropic and potential. This assumption is valid for flows with high Reynolds numbers in which boundary-layer separation does not occur, such as the flowfield around an airfoil (slender body moving parallel to its length) at low angles of attack. Taylor [5] introduced a coordinate transformation by which the governing acoustic equations in a steady low-Mach number homentropic potential flow are transformed into an ordinary wave equation. Taylor developed this transformation to aid aircraft noise measurements from wind-tunnel and low-speed flight tests. Taylor's transformation distorts the time variable and thereby decouples the mean-flow and acoustic equations. This is shown in Sec. II for external source scattering problems. Thus, the effect of a background flowfield on sound propagation can be obtained by solving, independently, the potential (Laplace) equation for steady fluid flow, and the Helmholtz equation for acoustic-wave propagation in the transformed time variable, and then transforming the result into the physical time variable. Astley and Bain [6] used Taylor's transform [5] in a similar way to arrive at the governing acoustic equations suitable for the

Presented as Paper 2996 at the 11th AIAA/CEAS Conference, Monterey, CA, 23–25 May 2005; received 8 August 2005; revision received 17 July 2006; accepted for publication 11 October 2006.

*Research Associate, Department of Engineering. Member AIAA.
†Professor and Head of the Energy, Fluid Mechanics and Turbomachinery Division, Department of Engineering. Member AIAA.

solution of Neumann boundary-value problems by boundary-element methods. Numerical solvers based on boundary-element methods are readily available for both Helmholtz and Laplace equations. Thus, existing boundary-element solvers can be used to solve the problem of sound propagation through low-Mach number homentropic potential flows. A boundary-element implementation by means of an example of acoustic scattering from a point source by a sphere immersed in a potential flow is described in Sec. III. The attractive feature of this technique is its simplicity. There are other advantages of using boundary-element methods to solve this problem. These will become apparent in Sec. III. In Sec. IV boundary-element solutions for two-dimensional models and comparisons with analytical models are presented. Calculations for a three-dimensional Silent Aircraft airframe are presented in Sec. V. At high acoustic frequencies, boundary-element methods become increasingly demanding (computationally). Thus, boundary-element calculations are restricted to low frequencies. These low-frequency calculations provide a lower bound for the acoustic shielding estimates.

II. Acoustic Scattering

Consider a configuration in which fluid having a steady freestream velocity of $\boldsymbol{u}_\infty$ flows past a fixed closed surface $\partial\Omega$. At low Mach numbers ($M^2 \ll 1$, where $M = |\bar{\boldsymbol{u}}|/c$ is the Mach number, $\bar{\boldsymbol{u}}$ is the local fluid velocity), the fluid flow can be considered to be incompressible (see Batchelor [7], pp. 167–168). Also, because variations in the speed of sound c depend on M^2, then correct to order M, c can be assumed to be a constant. Now if the fluid motion is assumed to be inviscid and irrotational, then the steady flow $\bar{\boldsymbol{u}}$ in the region Ω exterior to $\partial\Omega$ can be described by the Laplace equation

$$\nabla^2\bar{\phi} = 0 \tag{1}$$

with the requirement that the normal velocity on $\partial\Omega$ be zero. That is,

$$\boldsymbol{n}\cdot\nabla\bar{\phi} = 0 \quad \text{on } \partial\Omega \tag{2}$$

where $\boldsymbol{n}(\boldsymbol{x})$ is the unit inward normal at the point $\boldsymbol{x}$ on the surface $\partial\Omega$. Here $\bar{\phi}$ is the scalar velocity potential defined by $\bar{\boldsymbol{u}}(\boldsymbol{x}) = \nabla\bar{\phi}(\boldsymbol{x})$.

Equation (1) is the governing equation for the background (mean) flow. If this steady flow is disturbed by a small perturbation, the ensuing dynamics of the perturbed variables can be described by the continuity and momentum equations linearized about the equilibrium (mean/background) state given by the solution of Eq. (1). These linearized equations can then be manipulated such that for an acoustic source $S(\boldsymbol{x}, t)$, the unsteady potential acoustic field can be represented by a single equation in terms of the perturbation acoustic potential ϕ. For a low-Mach number mean flow, where terms of order M^2 are neglected, this equation is the convected wave equation (see Howe [8]):

$$\left(\frac{\partial}{\partial t} + \nabla\bar{\phi}\cdot\nabla\right)^2\phi - c^2\nabla^2\phi = S(\boldsymbol{x}, t) \tag{3}$$

For a rigid boundary, ϕ satisfies the boundary condition

$$\boldsymbol{n}\cdot\nabla\phi = 0 \quad \text{on } \partial\Omega \tag{4}$$

Although in this analysis $\partial\Omega$ is assumed to be a rigid surface, it can be generalized easily for surfaces with arbitrary impedances. In the far field, ϕ satisfies the Sommerfeld radiation condition [9] that, in spherical coordinates (r, θ, ψ), can be written as

$$\lim_{r\to\infty}\left[r\left(\frac{\partial\phi}{\partial r} + \frac{1}{c}\frac{\partial\phi}{\partial t}\right)\right] = 0 \tag{5}$$

To illustrate the solution technique, consider the time-harmonic Green's function $\phi_g(\boldsymbol{x}, t)$ that satisfies

$$\left(\frac{\partial}{\partial t} + \nabla\bar{\phi}\cdot\nabla\right)^2\phi_g - c^2\nabla^2\phi_g = \delta(\boldsymbol{x} - \boldsymbol{x_o})\exp(-\mathrm{i}\omega t) \tag{6}$$

The space-time Green's function g can be obtained by the following inverse Fourier transform:

$$g(\boldsymbol{x} - \boldsymbol{x_o}, t - t_o) = \frac{1}{2\pi}\int_{-\infty}^{\infty}\phi_g(\boldsymbol{x} - \boldsymbol{x_o}, t)\exp(\mathrm{i}\omega t_o)\,\mathrm{d}\omega \tag{7}$$

The solution to Eq. (3) is then given by a convolution of the space-time Green's function with the source $S(\boldsymbol{x}, t)$.

Using Taylor's transformations (see [5]):

$$\boldsymbol{X} = \boldsymbol{x}, \qquad T = t + \bar{\phi}/c^2 \tag{8}$$

$\phi_g(\boldsymbol{x}, t) = \Phi(\boldsymbol{X}, T)$, and neglecting terms of order M^2, where $M = |\nabla\bar{\phi}|/c$ is the Mach number, Eq. (6) transforms into

$$\left(\frac{\partial^2}{\partial T^2} - c^2\nabla_X^2\right)\Phi = \delta(\boldsymbol{X} - \boldsymbol{X_o})\exp[\mathrm{i}\omega\bar{\phi}(\boldsymbol{X})/c^2]\exp[-\mathrm{i}\omega T] \tag{9}$$

where $\nabla_X^2 = \partial^2/\partial X_i\partial X_i$. The boundary condition (4) transforms into

$$\boldsymbol{n}\cdot\left(\nabla_X\Phi + \frac{1}{c^2}\nabla\bar{\phi}\frac{\partial\Phi}{\partial T}\right) = 0 \quad \text{on } \partial\Omega \tag{10}$$

Upon substituting Eq. (2), the transformed boundary condition reduces to

$$\boldsymbol{n}\cdot\nabla_X\Phi = 0 \quad \text{on } \partial\Omega \tag{11}$$

Because the large time-asymptotic response is expected to be time-harmonic at the source frequency, the assumption $\Phi(\boldsymbol{X}, T) = \hat{\Phi}(\boldsymbol{X}; \omega)\exp[-\mathrm{i}\omega T]$ simplifies Eq. (9) into

$$(-\omega^2 - c^2\nabla_X^2)\hat{\Phi} = \delta(\boldsymbol{X} - \boldsymbol{X_o})\exp[\mathrm{i}\omega\bar{\phi}(\boldsymbol{X})/c^2] \tag{12}$$

The operator on the left-hand side is the familiar Helmholtz operator. Let the Green's function for the Helmholtz equation be given by

$$(-\omega^2 - c^2\nabla_X^2)\hat{\Phi}_h(\boldsymbol{X}|\boldsymbol{X}_s) = \delta(\boldsymbol{X} - \boldsymbol{X}_s) \tag{13}$$

with $\hat{\Phi}_h$ satisfying the boundary condition

$$\boldsymbol{n}\cdot\nabla_X\hat{\Phi}_h = 0 \quad \text{on } \partial\Omega \tag{14}$$

Then the solution to Eq. (12) is given by

$$\hat{\Phi}(X; \omega) = \hat{\Phi}_h(\boldsymbol{X}|\boldsymbol{X_o})\exp[\mathrm{i}\omega\bar{\phi}(\boldsymbol{X_o})/c^2] \tag{15}$$

Transforming back to the original variables, the time-harmonic Green's function is given by

$$\phi_g(\boldsymbol{x}, t) = \hat{\Phi}_h(\boldsymbol{x}|\boldsymbol{x_o})\exp\{\mathrm{i}\omega[\bar{\phi}(\boldsymbol{x_o}) - \bar{\phi}(\boldsymbol{x})]/c^2\}\exp(-\mathrm{i}\omega t) \tag{16}$$

The acoustic pressure is related to the perturbation potential via the Bernoulli equation

$$p(\boldsymbol{x}, t) = -\bar{\rho}\left(\frac{\partial\phi}{\partial t} + \nabla\bar{\phi}\cdot\nabla\phi\right) \tag{17}$$

where $\bar{\rho}$ is the freestream mean density.

With the acoustic potential given by Eq. (16), the acoustic pressure, correct to order M^2, can be written as

$$p(\boldsymbol{x}, t) = -\bar{\rho}(-\mathrm{i}\omega\hat{\Phi}_h + \nabla\bar{\phi}\cdot\nabla\hat{\Phi}_h)\exp\{\mathrm{i}\omega[\bar{\phi}(\boldsymbol{x_o}) - \bar{\phi}(\boldsymbol{x})]/c^2\}\exp(-\mathrm{i}\omega t) \tag{18}$$

Note that $\hat{\Phi}_h$ is independent of the mean flow. Its effect on the acoustic pressure is displayed, explicitly, through terms involving $\bar{\phi}(\boldsymbol{x})$.

III. Boundary-Element Formulation

The boundary-element implementation for the acoustic scattering problem involves a two-step process. From Eq. (16) it can be seen

that the magnitude of the complex acoustic potential is given by the solution of the Helmholtz equation, and the phase is a function of the mean flow. Because $\hat{\Phi}_h$ is independent of the mean flow, the acoustic potential and consequently the acoustic pressure field can be evaluated by solving, independently, the Helmholtz equation [(13) and (14)] and the Laplace equation [(1) and (2)]. Boundary-element methods for solving these equations are readily available. Thus the effect of low-Mach number homentropic potential flows on acoustic scattering problems can be obtained by using existing boundary-element software. Because acoustic and mean-flow calculations become decoupled, a single acoustic boundary-element calculation can be used to investigate a variety of mean flows, such as flows with different Mach numbers past airfoils at different angles of attack (if the source position remains fixed relative to the airfoil). Note that the mean-flow velocity potential need only be known at the source and observer positions, and it only affects the phase, not the sound pressure level. The effect of the mean flow on acoustic pressure only requires information of the mean-flow velocity at the observer's position. Hence, boundary-element methods are well-suited for solving the Laplace equation because they allow for pointwise computation of the flowfield. There are other advantages of using boundary-element methods. Radiation boundary conditions are implicitly satisfied and only the external surfaces of enclosed bodies in the domain (not the entire domain) need to be discretized. For problems in which there are several source locations but few observer locations of interest, an adjoint formulation can be used. This has a big computational advantage because the sound-propagation problem from multiple sources can be solved by a single calculation. It can be shown easily that the adjoint equation can be obtained from the direct Eq. (6) by just reversing the direction of the mean flow. Hence the same procedure already described with $\bar{\phi}$, replaced with $-\bar{\phi}$, can be used to obtain the adjoint solution.

To illustrate the application of the boundary-element method, we consider the example of the scattering of acoustic waves from a point source by a rigid sphere. Let the sphere of radius a be located at the origin and a point source be located on the x-axis at a distance r_s from the origin. The sphere is immersed in a flow with a uniform value of u_∞ in the $+x$ direction at infinity. Thus, both the mean flow and acoustic fields are axisymmetric about the x-axis. These fields can be described adequately by a spherical polar coordinate system (r, θ, ψ), as shown in Fig. 1.

As seen from Eq. (18), the pressure field for this problem requires a solution of both Helmholtz and Laplace equations. The solution of Laplace equation for this problem is well known and is given by (for a more general geometry, the solution could be obtained numerically by a boundary-element method)

$$\bar{\phi}(r, \theta) = u_\infty \cos\theta \left(\frac{a^3}{2r^2} + r \right) \tag{19}$$

The solution to Helmholtz equation ($\hat{\Phi}_h$) is obtained by using COMET/Acoustics [10]. The surface of the sphere is discretized by MSC/Patran [11]. Figure 2 compares the directivity pattern for $\hat{\Phi}_h$ at a distance of $kr = 200$, where $k = \omega/c$ is the source wave number, for different mesh resolutions, with the analytical solution. It can be seen that about ten mesh points per acoustic wavelength are adequate to yield a converged solution (cf. Agarwal and Morris [12]). The parameters chosen for this calculation are $ka = 2$, $kr_s = 4$, and $u_\infty = 0.2c$.

Once $\bar{\phi}$ and $\hat{\Phi}_h$ are known, the acoustic pressure field is obtained from Eq. (18). Figure 3 shows the sound directivity pattern in the axial plane at a distance of $kr = 200$. Also shown in the figure is the sound directivity pattern when the fluid is stationary. It can be seen that the flowfield enhances the pressure field in upstream directions and reduces it in downstream directions. Taylor [5] showed that the mean flow introduces a single Doppler factor $(1 - M_\infty \cos\theta)$ in the far-field expression for pressure, which explains the observed directivity patterns. A slightly modified derivation is presented here for completeness. In the far field, Eq. (18) can be simplified by noting that correct to order $1/r$,

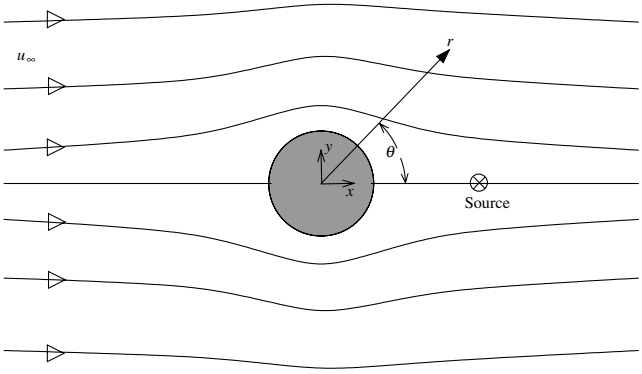

Fig. 1 Axial plane of a sphere immersed in a stream with a uniform velocity at infinity.

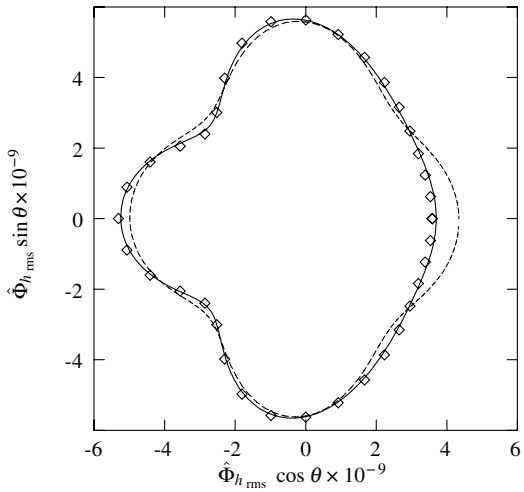

Fig. 2 Directivity pattern for $\hat{\Phi}_h$ ($ka = 2$, $kr_s = 4$, $kr = 200$. Solid line, 10 points per wavelength; dashed line, 6 points per wavelength; ◇, analytical solution).

$$\bar{\phi} = u_\infty r \cos\theta \tag{20}$$

and

$$\nabla^2 \hat{\Phi}_h = \frac{1}{r^2} \frac{\partial}{\partial r} \left(r^2 \frac{\partial \hat{\Phi}_h}{\partial r} \right) \tag{21}$$

Using (21), correct to order $1/r$, (13) can be written as

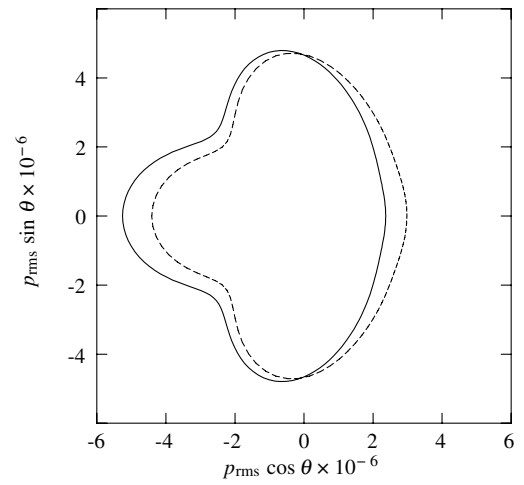

Fig. 3 Sound directivity pattern in the axial plane of the sphere (solid line, $u_\infty = 0.2c$; dashed line, $u_\infty = 0$).

$$-\omega^2\hat{\Phi}_h - c^2\frac{1}{r^2}\frac{\mathrm{d}}{\mathrm{d}r}\left(r^2\frac{\mathrm{d}\hat{\Phi}_h}{\mathrm{d}r}\right) = 0 \tag{22}$$

The distant outgoing wave solution to this equation is given by

$$\hat{\Phi}_h = \Lambda\frac{\exp[\mathrm{i}kr]}{r} \tag{23}$$

where Λ is independent of r. Upon substituting Eqs. (20) and (23) in Eq. (18) and neglecting terms of order $1/r^2$, it can be shown that

$$|p(\boldsymbol{x},t)| = \omega\bar{\rho}\hat{\Phi}_h(1 - M_\infty\cos\theta) \tag{24}$$

where M_∞ is the freestream Mach number. Equation (24) gives the effect of a potential mean flow on the far-field acoustic pressure amplitude. Note that this simple expression of single Doppler factor in the far-field expression for pressure is applicable only for a monopole source. For realistic sources, the effect of the flowfield on the sound directivity pattern would be more complex. The mean-flow convection effects for an arbitrary source distribution $\hat{S}(\boldsymbol{x})$ can be found by forming a convolution of the Green's function given by Eq. (16) with $\hat{S}(\boldsymbol{x})$. That is,

$$\begin{aligned}\phi(\boldsymbol{x};\omega) &= \int \phi_g(\boldsymbol{x}|\boldsymbol{x_o};\omega)\hat{S}(\boldsymbol{x_o})\,\mathrm{d}\boldsymbol{x_o}\\ &= \mathrm{e}^{-\mathrm{i}\omega\bar{\phi}(\boldsymbol{x})/c^2}\int \hat{\Phi}_h(\boldsymbol{x}|\boldsymbol{x_o})\exp[\mathrm{i}\omega\bar{\phi}(\boldsymbol{x_o})/c^2]\hat{S}(\boldsymbol{x_o})\,\mathrm{d}\boldsymbol{x_o}\end{aligned} \tag{25}$$

Defining a modified source distribution $\hat{S}'(\boldsymbol{x}) = \hat{S}(\boldsymbol{x})\times \exp[\mathrm{i}\omega\bar{\phi}(\boldsymbol{x})/c^2]$, Eq. (25) can be written as

$$\phi(\boldsymbol{x};\omega) = \mathrm{e}^{-\mathrm{i}\omega\bar{\phi}(\boldsymbol{x})/c^2}\left[\int \hat{\Phi}_h(\boldsymbol{x}|\boldsymbol{x_o})\hat{S}'(\boldsymbol{x_o})\,\mathrm{d}\boldsymbol{x_o}\right] \tag{26}$$

The term in the parentheses is the solution of the Helmholtz equation for the modified source distribution $\hat{S}'(\boldsymbol{x})$, which can be obtained by the boundary-element software. Finally, the pressure field is obtained by the application of Bernoulli's Eq. (18).

IV. Two-Dimensional Models

We expect that for an acoustic source placed above the wing, there would be a significant reduction of noise in the shadow region underneath the wing. To understand the effect of various parameters such as wing thickness, edge curvatures, source location, and frequency, we have analyzed two sets of two-dimensional wing models. One consists of a flat plate and a biconvex ellipse with sharp edges, as shown in Fig. 4, and the other consists of an ellipse and a Zhukovsky airfoil, shown in Fig. 5. These models have a chord length of $a = 2$ m. The ellipses have a maximum thickness of $2\epsilon = 0.1a$. The radius of curvature of the edge of the ellipse in Fig. 5, $\rho = \epsilon^2$, is chosen so as to match that of the leading edge of the airfoil. A time-harmonic point acoustic source is placed at $(0, 1.5\epsilon)$. The source frequency is chosen such that the Helmholtz number, $ka = 50$, where k is the wave number of the source. This Helmholtz number corresponds to the fundamental frequency of the fan of the Silent Aircraft engine, which is the lowest tonal frequency of interest. Because we expect more shielding at higher frequencies (as explained later), the present analysis provides a lower bound on the shielding estimates.

The two-dimensional acoustic shielding problem is solved by a boundary-element solver [12]. Because the wave equation is separable in elliptical coordinates, an analytical solution can be obtained for the ellipse and the flat plate, which is a zero-thickness ellipse. The analytical solution is given in Appendix A. It is consistent with the boundary-element solution. Figure 6 shows the sound directivity pattern for the flat plate and biconvex ellipse. Also shown is the directivity pattern for the incident field from the source. It can be seen that there is a reduction of noise by about 13 dB noise reduction underneath the wing compared with the incident field. The directivity pattern has some interesting features. There are wiggles

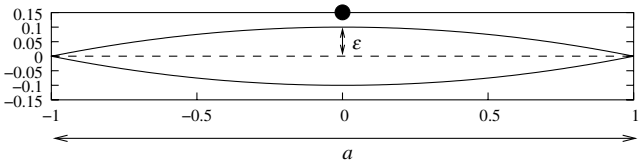

Fig. 4 2-D wing models: flat plate (dashed line) and a biconvex ellipse (solid line).

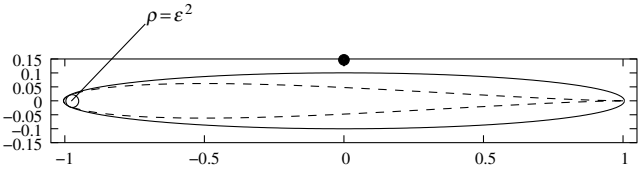

Fig. 5 2-D wing models: Zhukovsky airfoil (dashed line) and an ellipse (solid line).

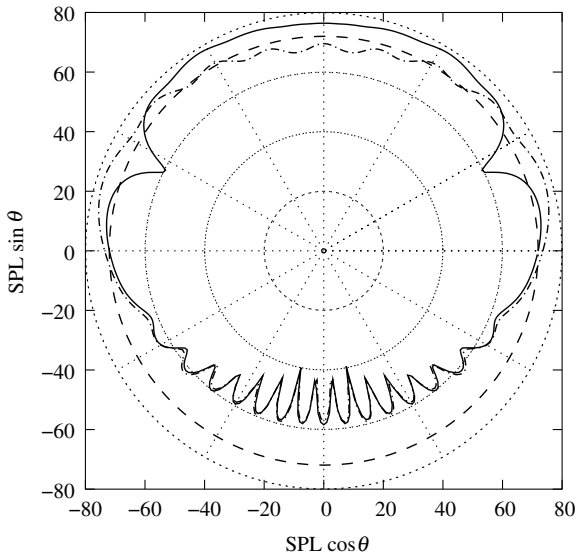

Fig. 6 Sound directivity pattern from the flat plate (solid line), biconvex cylinder (dash-dot line), and the incident field (dashed line).

(lobes) in the shadow region underneath the wing, which are almost identical for the flat plate and the biconvex ellipse. There are dips in the directivity pattern above, for the flat plate. The dips are due to the interference between the direct and reflected waves between the source and the observer. This can be seen easily by placing an image source below the flat plate that is of the same strength and is equidistant from the plate. The image source accounts for the reflected waves from the upper surface of the wing. The sound field obtained by adding the contribution from the source and image, shown in Fig. 7, has dips in the directivity pattern at the same location as that given by the boundary-element solution. The dips disappear for the biconvex-ellipse case, because in that case the source is closer to the surface, hence the source and image pair being closer compared to a wavelength, behave nearly as a single source (the phase difference is small). The wiggles underneath are due to the interference from the diffracted field from the two edges. The high value for the Helmholtz number ($ka = 50$) indicates that the acoustic wavelength is small compared with the chord length. Therefore, for the length scales associated with this problem, the frequency is high and hence ray-theory results are applicable. The two-dimensional diffracted field from the edge of a wedge with exterior angle β is given by (see Appendix B and Fig. B1)

$$\hat{p}_{2D} = \frac{\hat{S}}{k}\frac{\pi}{\beta}\frac{\mathrm{i}}{\sqrt{rr_s}}\mathrm{e}^{\mathrm{i}k(r+r_s)}D_v(\phi,\phi_s) \tag{27}$$

where (r,ϕ) and (r_s,ϕ_s) are the locations of the observer and source,

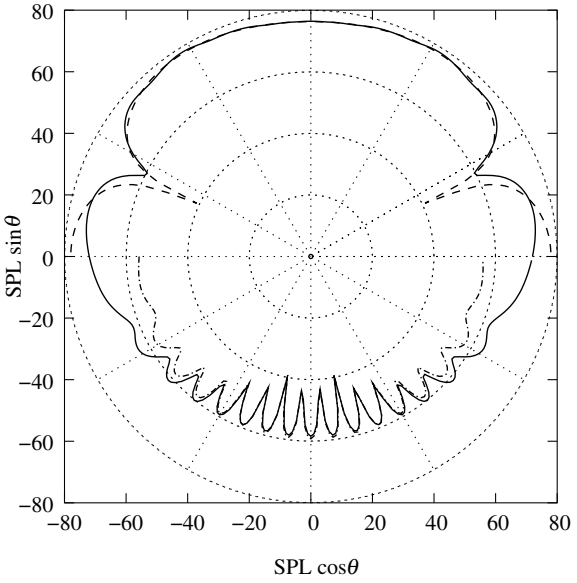

Fig. 7 Comparison between the interference pattern obtained from the image-source model (dashed line) and the diffraction field in the shadow zone (dash-dot line) with the boundary-element solution (solid line).

respectively, in polar coordinates with the origin at the edge, $\hat{S}$ is the source strength, and $D_v(\phi, \phi_s)$ is the directivity function defined in Eq. (B2). The total diffracted field in the shadow region, given by adding the contributions from the two edges, is shown in Fig. 7. The interference pattern from the diffracted field matches the directivity pattern underneath the plate obtained from the boundary element solutions. Note that the only difference in the expression for the diffracted field between the flat plate and the biconvex ellipse is the external wedge angle β. For the flat plate, $\beta = 2\pi$, which is nearly the same for the biconvex ellipse. This explains why the diffracted field for the two cases is similar. It can be seen from Eq. (27) that the diffracted pressure field in the shadow region is inversely proportional to frequency. Thus, if the frequency is doubled, sound pressure level (SPL) reduces approximately by 6 dB. Note that doubling the frequency would double the number of lobed patterns, but, averaged over a wavelength, the SPL would reduce by 6 dB. In three dimensions, the diffracted pressure field is inversely proportional to square root of frequency [see Eq. (B1)]. Thus doubling the frequency would reduce the SPL by approximately 3 dB.

Figure 8 shows the sound directivity pattern for the ellipse and the Zhukovsky airfoil. The directivity pattern looks similar to the flat-plate and biconvex-ellipse cases, even though the Zhukovsky airfoil has a rounded leading edge and the ellipse has rounded leading and trailing edges. This indicates that the sharp-edge-diffraction mechanism is applicable also to the rounded-edge models. This is because the radius of curvature ρ is small compared with the wavelength ($k\rho = 0.25$). However, as the frequency of the source increases, $k\rho$ would become larger and the diffraction mechanism would change from a sharp-edge to a creeping-ray mechanism. The pressure field due to sharp-edge-diffraction falls linearly in two dimensions with increasing frequency, whereas it decays exponentially for a creeping wave. Thus, for rounded edges with nonnegligible $k\rho$, a significantly higher reduction of sound in the shadow region can be expected. This is the subject of ongoing research work in which high-frequency acoustic scattering is being calculated by ray-tracing techniques. The dissimilarities in the interference pattern in the forward arc (lower-left quadrant) in Fig. 8 can be understood by evaluating the difference in the length of the paths around the two edges from the source to an observer. At a given observer location, let this path difference be represented by a phase difference $\Delta\phi$. It can be shown that the difference between $\Delta\phi$ for the Zhukovsky airfoil and the ellipse $[(\Delta\phi)_{\text{zhukovsky}} - (\Delta\phi)_{\text{ellipse}}]$ is greater for observer locations in the forward arc than in the rearward arc.

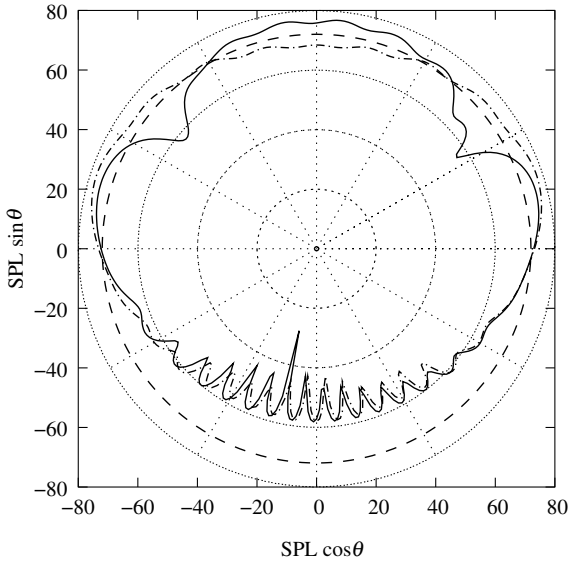

Fig. 8 Sound directivity pattern from an ellipse (dash-dot line) and a Zhukovsky airfoil (solid line).

To determine the effect of source location on the amount of shielding in the shadow region, it is appropriate to solve the adjoint problem. Figure 9 shows the adjoint sound field above the Zhukovsky airfoil for three source locations in the far field. In polar coordinates, the sources are located at $kr = 500$ and $\theta = -90$, -60, and -120 deg. The origin of the coordinate system is on the centerline of the airfoil at $x = 0$. Angles are measured positive in a counterclockwise direction. $\theta = 0$ deg corresponds to the positive x-axis. Thus, $\theta = -90$ deg is directly underneath the airfoil, -60 deg is towards the rear of the aircraft, and -120 deg is in front. Because of the reciprocity between the adjoint and direct fields, the adjoint sound field at an observer location above the airfoil from a source in the far field is the same as the direct sound field from the source located above the airfoil and the observer in the far field. That is, $p(\boldsymbol{x}|\boldsymbol{x}_s) = p_a(\boldsymbol{x}_s|\boldsymbol{x})$, where p and p_a are the direct and adjoint fields, respectively, $\boldsymbol{x} \equiv (r, \theta)$ is the observer location, and $\boldsymbol{x}_s$ is the source location. Figure 9 also shows the adjoint incident field from the far-field source located at $\theta = -90$ deg. In general, the amount of shielding is a function of the relative locations of source and observers with respect to the edge. It can be seen that unless the source is located very close to the edges, significant amount of shielding is obtained in all directions. This can be explained based on the edge-diffraction theory. If there is no direct line of sight between the source and observer, then the observer is in the shadow region and it receives a weak diffracted field from the edges.

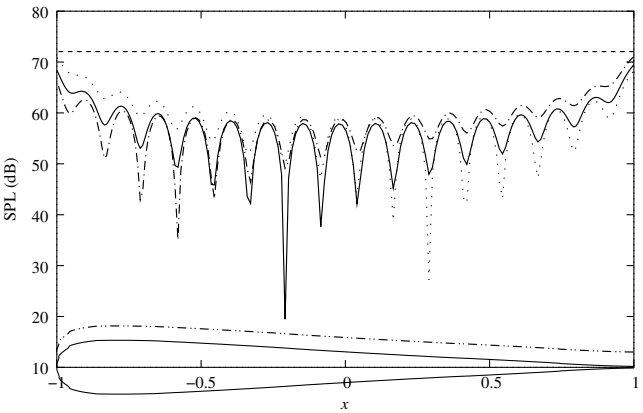

Fig. 9 SPLs for the adjoint acoustic field at a location (dash-dot-dot line) above the Zhukovsky airfoil for three far-field source locations: solid line, $\theta = -90$ deg; dash-dot line, $\theta = -60$ deg; dotted line, $\theta = -120$ deg; dashed line, incident field.

V. Acoustic Shielding by a Silent Aircraft

Acoustic shielding effects are estimated by means of a monochromatic point acoustic source placed above the airframe of Silent Aircraft Experimental (SAX03). Figure 10 shows the orthographic projections of the SAX03 airframe. The source is located at $(2a/3, 0, 0.05a)$, where a is the center-body chord length.

Figure 11 shows the far-field sound directivity patterns in the x–z plane at three spanwise locations: $y = 0$, $y = b/2$, and $y = b$, where b is the wingspan. Also shown is the incident field from the source on the plane $y = 0$. The source frequency corresponds to a Helmholtz number, $ka = 50$. This frequency corresponds to the fundamental frequency of the fan (shaft frequency) [13]. It can be seen that a reduction of at least 5 dB is obtained in the shadow region underneath the aircraft. This can be seen clearly in Fig. 12, which shows the shielding contour levels on the ground, 232 m below the aircraft. The contour levels represent the difference between the total and incident acoustic fields. Thus, the negative levels indicate the amount of shielding. There are isolated regions on the ground with large amounts of shielding. This is due to the destructive interference effects from the multiple diffracted rays reaching a particular observer on the ground. Note that we obtain less shielding directly below the aircraft ($y = 0$ in Fig. 11) compared with observers off to the side, even though we would expect that the wing would block the line of sight to the source more effectively directly below the aircraft. This is due to the symmetry of the problem. The source is placed symmetrically above the wing, so the acoustic contributions from the various edges add up constructively directly below the aircraft. In dimensional terms, the frequency of the source for this calculation is approximately 50 Hz. The perceived forward-propagating engine noise is very small at such low frequencies. At higher frequencies, where the engine noise is more important, we expect a greater amount of noise reduction due to shielding, as explained in the preceding section.

VI. Conclusions

Acoustic shielding of low-frequency engine noise by the Silent Aircraft airframe has been investigated by solving an external acoustic scattering problem. By means of Taylor's transformation, the governing equations for sound propagation through homentropic potential flows at low Mach numbers can be transformed into an ordinary wave equation. For external acoustic scattering problems from time-harmonic sources, Taylor's transformation decouples the mean-flow and acoustic-field calculations. The acoustic potential field can then be obtained by solving, independently, the Helmholtz and Laplace equations. This technique is amenable to solving both direct and adjoint sound-propagation problems. An adjoint solution can be obtained by solving the corresponding direct problem after reversing the direction of the mean flow and swapping the source and observer locations. Boundary-element methods offer a simple and efficient way of solving these equations at low frequencies. Analysis of simple two-dimensional models has shown that there are two important length scales in the scattering problem: the chord length and the radius of curvature of the edges. For the engine frequencies in the audible range, even the lowest frequency corresponds to an acoustic wavelength that is much smaller than the chord length. This means that models based on ray theory can be used to get better physical insight into the boundary-element solutions. It has been observed that if the radius of curvature of an edge is small compared to an acoustic wavelength, then the edge behaves as a sharp edge. If there is no direct line of sight between a source above the wing and an observer underneath, then the observer is in a shadow region where

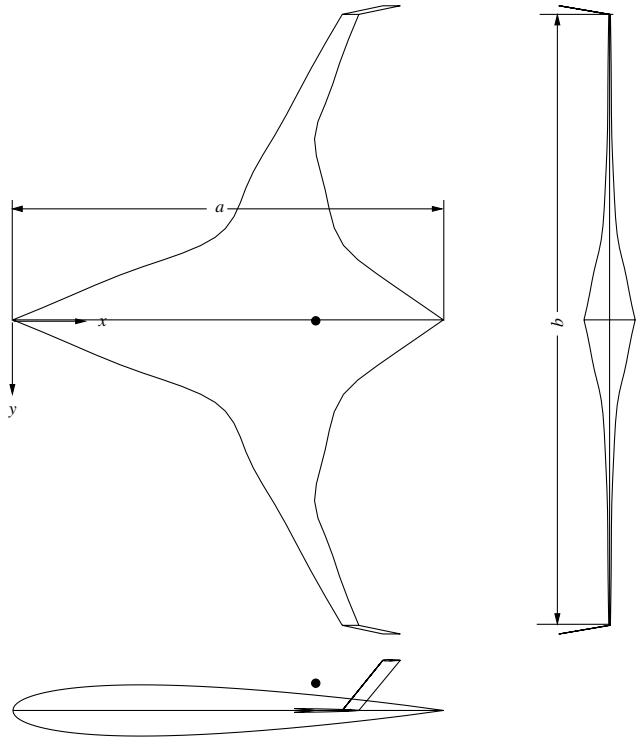

Fig. 10 Orthographic projections of the Silent Aircraft airframe SAX03 (from Diedrich [14]).

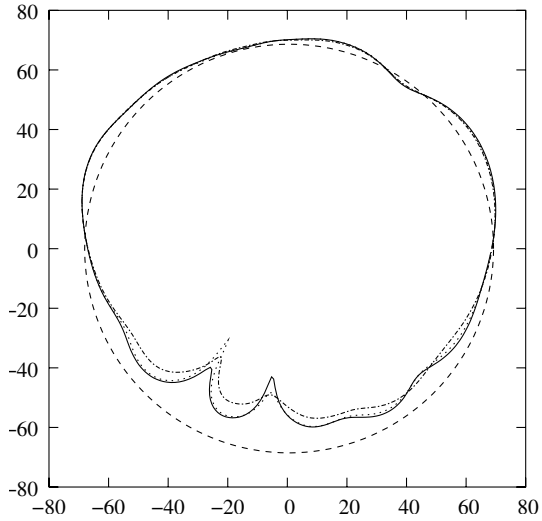

Fig. 11 Sound directivity pattern in the far field ($kr = 500$) for SAX03. Dashed line, incident field; solid line, $y = 0$; dotted line, $y = b/2$; dash-dot line, $y = b$.

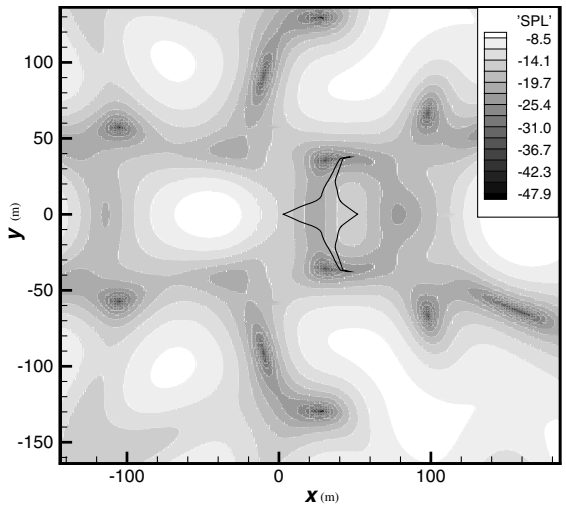

Fig. 12 Shielding contour levels on the ground for SAX03, height 232 m.

there is a significant amount of noise reduction. The sound pressure field in the shadow region is inversely proportional to frequency for two-dimensional problems and to square root of frequency for three-dimensional problems. Therefore, acoustic shielding becomes more effective at higher frequencies. Low-frequency calculations of acoustic shielding from a monopole source, pulsating at the fundamental fan frequency, placed above a Silent Aircraft airframe, show a significant amount of shielding (at least 5 dB) throughout the shadow region. Boundary-element methods become increasingly demanding of computational resources at high frequencies. To complement the boundary-element method at high frequencies, a solution procedure based on ray acoustics is being developed.

Appendix A: Acoustic Scattering from an Ellipse

The time-harmonic Green's function satisfies the Helmholtz equation

$$(\nabla^2 + k^2)G(\boldsymbol{r}|\boldsymbol{r_o};\omega) = -4\pi\delta(\boldsymbol{r}-\boldsymbol{r_o}) \tag{A1}$$

Consider an elliptic coordinate system (see Fig. A1) defined by

$$x = a/2\cosh\mu\cos\nu \qquad y = a/2\sinh\mu\sin\nu \tag{A2}$$

The incident field from the point source can be expanded in terms of a series in elliptical coordinates (see p. 1421, Morse and Feshbach [15])

$$\begin{aligned} G^I(\boldsymbol{r}|\boldsymbol{r_o};\omega) &= \mathrm{i}\pi H_0^{(1)}(kR) \\ &= 4\pi\mathrm{i}\left\{\sum_{m=0}^{\infty}\left[\frac{Se_m(h,\cos\nu_o)}{M_m^e(h)}\right]Se_m(h,\cos\nu)\right. \\ &\quad\times\begin{cases} Je_m(h,\cosh\mu_o)He_m(h,\cosh\mu); & \mu>\mu_o \\ Je_m(h,\cosh\mu)He_m(h,\cosh\mu_o); & \mu_o>\mu \end{cases} \\ &\quad+\sum_{m=1}^{\infty}\left[\frac{So_m(h,\cos\nu_o)}{M_m^o(h)}\right]So_m(h,\cos\nu) \\ &\quad\left.\times\begin{cases} Jo_m(h,\cosh\mu_o)Ho_m(h,\cosh\mu); & \mu>\mu_o \\ Jo_m(h,\cosh\mu)Ho_m(h,\cosh\mu_o); & \mu_o>\mu \end{cases}\right\} \end{aligned} \tag{A3}$$

where

$$He_m = Je_m + \mathrm{i}Ne_m \qquad Ho_m = Jo_m + \mathrm{i}No_m \tag{A4}$$

are solutions corresponding to outgoing waves; Se_m, So_m are the even and odd Mathieu functions, respectively, of order m; $M_m^e(h)$, $M_m^o(h)$ are the normalization constants for these functions; Je_m, Jo_m are the even and odd radial Mathieu functions of the first kind; and Ne_m, No_m are the even and odd radial Mathieu functions of the second kind.

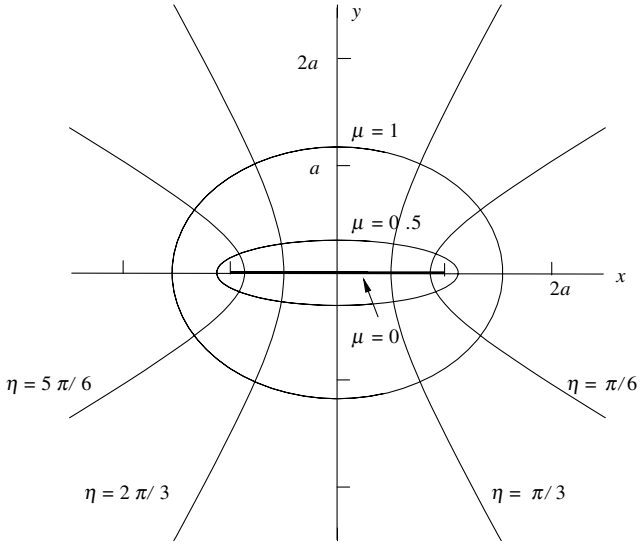

Fig. A1 Elliptic coordinates.

The scattered field can be represented as

$$\begin{aligned} G^S(\mu,\nu|\mu_o,\nu_o) &= \sum_{m=0}^{\infty}A_m^e(\mu_o,\nu_o)Se_m(h,\cos\nu)He_m(h,\cosh\mu) \\ &\quad+\sum_{m=1}^{\infty}A_m^o(\mu_o,\nu_o)So_m(h,\cosh\nu)Ho_m(h,\cosh\mu) \end{aligned} \tag{A5}$$

$$\begin{aligned} \frac{\partial G^S}{\partial\mu}(\mu=0) &= \sum_{m=0}^{\infty}A_m^e Se_m(h,\cos\nu)Je_m(h,1) \\ &\quad+\sum_{m=1}^{\infty}A_m^o So_m(h,\cos\nu)Ho_m'(h,1) \end{aligned} \tag{A6}$$

From Eq. (A3),

$$\begin{aligned} &\frac{\partial G^I}{\partial\mu}(\mu=0) \\ &=4\pi\mathrm{i}\sum_{m=1}^{\infty}\left[\frac{So_m(h,\cos\nu_o)}{M_m^o(h)}\right]So_m(h,\cos\nu)Jo_m'(h,1)Ho_m(h,\cosh\mu_o) \end{aligned} \tag{A7}$$

Because the normal velocity on the plate must be zero

$$\frac{\partial G^S}{\partial\mu}(\mu=0) = -\frac{\partial G^I}{\partial\mu}(\mu=0) \tag{A8}$$

This gives

$$\begin{aligned} A_m^e &= 0 \\ A_m^o &= -4\pi\mathrm{i}\left[\frac{So_m(h,\cos\nu_o)}{M_m^o(h)}\right]\frac{Jo_m'(h,1)}{Ho_m'(h,1)}Ho_m(h,\cosh\mu_o) \end{aligned} \tag{A9}$$

Hence

$$\begin{aligned} G^S &= -4\pi\mathrm{i}\frac{Jo_m'(h,1)}{Ho_m'(h,1)}\left[\frac{So_m(h,\cos\nu_o)}{M_m^o(h)}\right] \\ &\quad\times So_m(h,\cos\nu)Ho_m(h,\cosh\mu_o)Ho_m(h,\cosh\mu) \end{aligned} \tag{A10}$$

Finally

$$G(\boldsymbol{r}|\boldsymbol{r_o};\omega) = G^I + G^S \tag{A11}$$

Appendix B: Diffracted Field from a Two-Dimensional Edge

Consider a rigid wedge with a sharp edge. The edge of the wedge coincides with the z-axis. Let the observer location in a cylindrical coordinate system be given by (r,ϕ,z), where the polar angle $\phi = 0$ corresponds to one of the faces of the wedge and $\phi = \beta$ corresponds to the other face, as shown in Fig. B1. A time-harmonic monopole source of amplitude $\hat{S}$ and wave number k is located at (r_s,ϕ_s,z_s). The expression for the diffracted field by the edge of the wedge in a three-dimensional space is given by (see Pierce [9], p. 491)

$$\hat{p}_{\,3\mathrm{D}} = \frac{\hat{S}}{2\beta}\left(\frac{2\pi}{kLrr_s}\right)^{1/2}\mathrm{e}^{\mathrm{i}(kL+\pi/4)}D_\nu(\phi,\phi_s) \tag{B1}$$

where

$$D_\nu(\phi,\phi_s) = \frac{\sin\nu\pi}{\cos\nu\pi-\cos\nu(\phi+\phi_s)} + \frac{\sin\nu\pi}{\cos\nu\pi-\cos\nu(\phi-\phi_s)} \tag{B2}$$

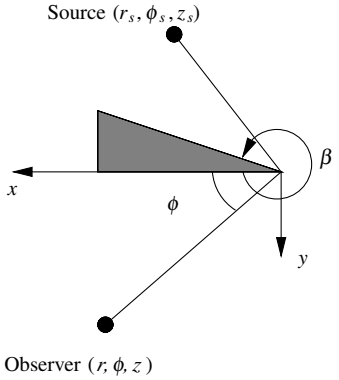

Fig. B1 Parameters for diffraction from a sharp edge.

$L = [(r + r_s)^2 + (z - z_s)^2]^{1/2}$ is the shortest path around the edge from the source to the observer, and $\nu = \pi/\beta$ is the wedge index.

The corresponding diffracted field in two dimensions can be obtained by replacing the point source by a line source of strength $\hat{S}$ per unit length. Then the two-dimensional diffracted field is given by

$$\hat{p}_{2D} = \int_{-\infty}^{\infty} \hat{p}_{3D}\, \mathrm{d}z_s \tag{B3}$$

Without loss of generality z is chosen to be zero. This integrand has an exponential term with an imaginary argument. This can be integrated by the method of stationary phase for large kL (or large kr). After the application of the method of stationary phase, the expression for the two-dimensional diffracted field is given by

$$\hat{p}_{2D} = \frac{\hat{S}}{k}\frac{\pi}{\beta}\frac{\mathrm{i}}{\sqrt{rr_s}}\mathrm{e}^{\mathrm{i}k(r+r_s)}D_\nu(\phi, \phi_s) \tag{B4}$$

Acknowledgments

This work is supported by Cambridge-MIT Institute (CMI) as part of the "Silent Aircraft Initiative." The authors would like to thank Andrew Faszer for his help with Pro-Engineer, Daniel Crichton for providing the fan noise data, and James Hileman and Patrick Freuler for providing the CAD model for SAX03.

References

[1] Jeffery, R. W., and Holbeche, T. A., "Experimental Studies of Noise-Shielding Effects for a Delta-Winged Aircraft," AIAA Paper 75-513, 1975.

[2] Clark, L. R., and Gerhold, C. H., "Inlet Noise Reduction by Shielding for the Blended-Wing-Body Air-Plane," AIAA Paper 99-1937, 1999.

[3] Gerhold, C. H., Clark, L. R., Dunn, M. H., and Tweed, J., "Investigation of Acoustical Shielding by a Wedge-Shaped Airframe," AIAA Paper 2004-2866, 2004.

[4] Ricouard, J., Davy, R., Loheac, P., Moore, A., and Piccin, O., "ROSAS Wind Tunnel Test Campaign Dedicated to Unconventional Aircraft Concepts Study," AIAA Paper 2004-2867, 2004.

[5] Taylor, K., "A Transformation of the Acoustic Equation with Implications for Wind-Tunnel and Low-Speed Flight Tests," *Proceedings of the Royal Society of London. Series A, Mathematical, Physical, and Engineering Sciences*, Vol. 363, No. 1713, 1978, pp. 271–281.

[6] Astley, R. J., and Bain, J. G., "A Three-Dimensional Boundary Element Scheme for Acoustic Radiation in Low Mach Number Flows," *Journal of Sound and Vibration*, Vol. 109, No. 3, 1986, pp. 445–465.

[7] Batchelor, G. K., *An Introduction to Fluid Dynamics*, Cambridge University Press, Cambridge, England, 1967.

[8] Howe, M. S., "The Generation of Sound by Aerodynamic Sources in an Inhomogeneous Steady Flow," *Journal of Fluid Mechanics*, Vol. 67, 1975, pp. 597–610.

[9] Pierce, A. D., *Acoustics, An Introduction to Its Physical Principles and Applications*, American Institute of Physics, New York, 1994.

[10] COMET/Acoustics, User's Manual, Collins & Aikman, Ann Arbor, MI, 2003.

[11] MSC/Patran, User's Manual, The MacNeaSchwendler Corporation, Santa Ana, CA, 2003.

[12] Agarwal, A., and Morris, P. J., "Prediction Method for Broadband Noise from Unsteady Flow in a Slat Cove," *AIAA Journal*, Vol. 44, No. 2, 2006, pp. 301–310.

[13] Hall, C. A., and Crichton, D., "Engine and Installation Configurations for a Silent Aircraft," ISABE Paper 2005-1164, 2005.

[14] Diedrich, A., "The Multidisciplinary Design and Optimization of an Unconventional, Extremely Quiet Transport Aircraft," M.S. Thesis, Dept. of Aeronautics and Astronautics, Massachusetts Institute of Technology, Cambridge, MA, 2005.

[15] Morse, P. M., and Feshbach, H., *Methods of Theoretical Physics*, Vol. 2, McGraw–Hill, New York, 1953.

K. Ghia
Associate Editor